RESEARCH ARTICLE | JUNE 01 2022

Wall heat flux in a supersonic shock wave/turbulent boundary layer interaction

Fulin Tong (童福林); Xianxu Yuan (袁先旭); Jiang Lai (赖江); ... et. al

Physics of Fluids 34, 065104 (2022)
https://doi.org/10.1063/5.0094070

Physics of Fluids ARTICLE scitation.org/journal/phf

Wall heat flux in a supersonic shock wave/turbulent boundary layer interaction

Cite as: Phys. Fluids **34**, 065104 (2022); doi: 10.1063/5.0094070
Submitted: 31 March 2022 · Accepted: 15 May 2022 ·
Published Online: 1 June 2022

View Online Export Citation CrossMark

Fulin Tong (童福林),[1] Xianxu Yuan (袁先旭),[1] Jiang Lai (赖江),[1] Junyi Duan (段俊亦),[2,3] Dong Sun (孙东),[1] and Siwei Dong (董思卫)[1,a)]

AFFILIATIONS

[1]State Key Laboratory of Aerodynamics, 621000 Mianyang, China
[2]LHD, Institute of Mechanics, Chinese Academy of Sciences, 100190 Beijing, China
[3]School of Engineering Science, University of Chinese Academy of Sciences, 100049 Beijing, China

[a)]Author to whom correspondence should be addressed: siwei.dong@cardc.cn

ABSTRACT

The characteristics of wall heat flux (WHF) beneath a supersonic turbulent boundary layer interacting with an impinging shock wave with a 33.2° angle at Mach 2.25 are analyzed using direct numerical simulation. It is found that the QP85 scaling, defined as the ratio of the mean WHF and wall pressure, changes across the interaction. The probability density function of the WHF fluctuations normalized by the local root-mean-squared value is similar to that of wall shear stress. Comparing the WHF and wall pressure spectra shows that the low-frequency shock unsteadiness exhibits little influence on the spectrum. The space–time correlation of the fluctuating WHF reveals that both the streamwise correlation length scale and the convection velocity experience a sharp decrease in the separation region and subsequent recovery in the downstream region. Moreover, the mean WHF in an incident shock interaction is decomposed for the first time. An analysis of the velocity and temperature fluctuations based on bidimensional empirical mode decomposition is performed to evaluate the contribution of turbulent structures with specific spanwise length scales to the mean WHF generation. The decomposed results indicate that the contribution associated with the large-scale structures in the outer region is greatly amplified by the shock interaction and has the leading role in the generation downstream of the interaction.

I. INTRODUCTION

Shock wave and turbulent boundary layer interaction (SWTBLI) has great practical relevance in a wide range of high-speed aircraft aerodynamic and thermodynamic designs. It causes maximum surface fluctuating pressure, severe wall heat flux (WHF) peak, and strong unsteadiness, causing significant adverse impacts on aircraft performance. Despite numerous experimental and numerical studies conducted over the last two decades and remarkable progress associated with the fundamental phenomena involved, a deeper physical understanding of the wall-flow variables involved in SWTBLIs is needed, particularly regarding wall heat flux. It is well known that the increased peak heating rates in strong interactions can be about 10–100 times the values in the incoming undisturbed boundary layer flow, even much larger than the equivalent stagnation point value, as reviewed by Dolling[1] and Gaitonde.[2] Consequently, the accurate prediction of heat transfer rate is essential to the thermal protection system design of supersonic and hypersonic vehicles.

The WHF in canonical SWTBLIs has been extensively studied by experiments and Reynolds-averaged Navier–Stokes (RANS) simulations for a wide range of Mach and Reynolds numbers. Most of these researches focused on the time-averaged WHF because of measurement difficulties and modeling limitations in obtaining the fluctuating WHF. For example, Bushnell and Weinstein[3] used the concept of a viscous sublayer to propose a reasonable correlation for the peak heating in experimental data for turbulent interactions with separation at $4 \leq M_\infty \leq 6$. In experiments of turbulent boundary layers interacting with shock and expansion waves, Back and Cuffel[4] found that the WHF scaled with the wall pressure and suggested an empirical power-law dependence with the exponent 0.85 to reasonably describe the relationship between surface quantities. Later, this scaling was further supported by Murray *et al.*[5] in axisymmetric hypersonic SWTBLIs. Applying the quantitative infrared thermography technique, Schülein[6] experimentally studied the influence of increased shock strength on skin friction and WHF behavior. They showed that the Stanton

number increased less rapidly than the skin friction and revealed that the analogy between momentum and heat transfer was not valid in the interaction region. Numerically, Lee *et al.*[7] investigated the heat transfer in five swept shock wave/turbulent boundary layer interactions using a k–ε turbulence model, suggesting a simple quasi-conical correlation for the peak heating. Pasha and Juhany[8] adopted the k–ω turbulence model with a shock unsteadiness modification and variable Prandtl number to perform a parametric study of heat transfer rate in a compression ramp at Mach 9. Li *et al.*[9] used RANS solutions to propose new peak pressure–heat flux correlations for shock interactions on V-shaped blunt leading edges. Despite these striking advances, the generation mechanism of the mean peak heating rate is not entirely understood, especially in the reattachment region of the interaction.

One objective of the present study is to provide a physical interpretation of the mean peak WHF generation in the reattachment region of an incident shock interaction, using heat flux decomposition and bidimensional empirical mode decomposition (BEMD). Importantly, Sun *et al.*[10] proposed a decomposition formula for the heat flux coefficient by integrating the total energy equation, decomposing the WHF in a hypersonic transitional boundary layer at $M_\infty = 6.0$. Their decomposition suggested that the work done by the molecular stress and the Reynolds stresses dominated the WHF production.

Recently, Tong *et al.*[11] extended this method to a supersonic turbulent boundary layer with a cold wall thermal condition. Furthermore, they applied the BEMD to quantify the contribution of the fluctuating velocity and temperature structures with specific spanwise length scales to the mean WHF. It was argued that the mean WHF generation was associated with the combined action of near-wall small-scale structures and large-scale structures in the logarithmic and outer regions. The present study performs (for the first time to the authors' knowledge) the mean WHF decomposition in the reattachment region of SWTBLIs and quantifies the contribution of the turbulence structures related to the generation.

There has been very limited research to date dealing with the fluctuating WHF in the interaction region using direct numerical simulation (DNS). In particular, the influence of the unsteady shock motion on the pre-multiplied fluctuating WHF spectra was investigated in the DNS studies of an incident shock interaction at Mach 2.28 by Bernardini *et al.*[12] Significant differences from earlier studies[13–15] of wall pressure spectra were reported. In their spectral analysis, the intermediate-/high-frequency energy was predominant across the interaction, and no evident low-frequency dynamics were observed. They concluded that the low-frequency shock motion exhibited little influence on the WHF spectra and suggested that the shedding of vortical structures in the separated shear layer developing in the first part of the interaction could explain the shift toward intermediate frequencies. In follow-up work, Volpiani *et al.*[16] found that the effect of wall cooling and wall heating on the WHF spectra was very different. A comparative quantitative analysis showed that decreasing the wall temperature led to a weak interaction, and no frequency shift was observed. By contrast, the heated case corresponded to a stronger interaction, and the spectra displayed similar behavior to those of Bernardini *et al.*[12] However, no quantitative information related to the spatial and temporal evolution of the WHF fluctuation fields in SWTBLIs has yet been reported in the literature.

In the present work, we perform a baseline DNS of an impinging oblique shock wave interacting with a supersonic turbulent boundary layer spatially developing over a cold flat plate at Mach 2.25. The resulting DNS database is analyzed in detail to characterize the statistical properties of the fluctuating WHF and uncover the mean WHF generation mechanism downstream of the interaction. The present study accurately captures both the full range of turbulent flow scales and the unsteady WHF signals to improve the physical understanding of the WFH in SWTBLIs.

This paper is structured as follows. In Sec. II, the simple flow configuration selected for the DNS and the computational setup adopted are fully described. Section III discusses the structure of the WHF field through analyses of the probability density function, power spectral density (PSD), space–time correlations, and mean WHF decomposition. Finally, concluding remarks are offered in Sec. IV.

II. NUMERICAL METHODOLOGY

A. Flow configuration

A sketch of the rectangular computational domain plotted in the Cartesian coordinates (x, y, z) is shown in Fig. 1. The domain has dimensions $L_x \times L_y \times L_z = 99.6 \times 10.2 \times 4.4\,\text{mm}^3$ in the streamwise (x), wall-normal (y), and spanwise (z) directions, respectively. A spatially developing supersonic turbulent boundary layer over an isothermal cold flat plate, generated by the laminar-to-turbulent transition method of Pirozzoli *et al.*,[17] is impinged upon by an oblique shock wave with a 33.2° angle. A region of blowing and suction disturbances, extending from $x_a = 7.5$ mm to $x_b = 20.2$ mm, is applied at the wall to trip the transition.

A shock generator is not included. Instead, following the recent simulations of Fang *et al.*[18] and Pasquariello *et al.*,[19] the Rankine–Hugoniot relations are imposed at the upper boundary of the domain to numerically generate the impinging shock at the nominal impingement point $x_s = 71.1$ mm. The free-stream temperature and Reynolds number based on the boundary layer thickness δ at the reference point $x_{ref} = 63.5$ mm are $T_\infty = 169.44$ K and $Re_\delta = 31\,753$, which are in good agreement with the recent DNS study of Tong *et al.*[11] The selected wall temperature is $T_w = 254.16$ K, corresponding to 0.75 times the recovery temperature T_r. Throughout this paper, the subscripts "∞" and "w" refer to the free-stream parameters and the wall

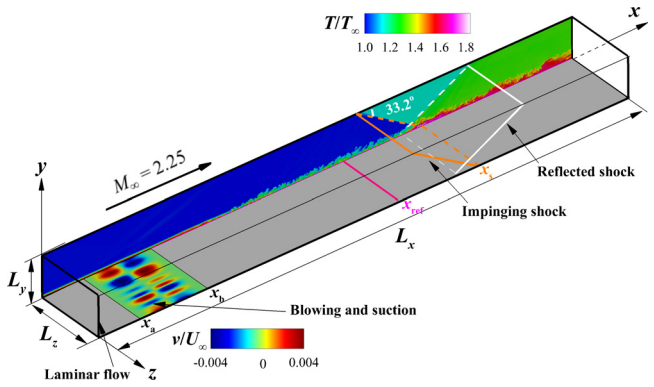

FIG. 1. Illustration of the computational domain with temperature contours in the x-y plane and wall-normal velocity in the wall blowing and suction region. The variable x_s denotes the nominal shock impingement; x_{ref} is the reference station; x_a and x_b are the start and endpoints of the blowing and suction regions, respectively.

values, respectively, and δ denotes the thickness of the upstream turbulent boundary layer at x_{ref}.

B. Computational setup

In the simulation, the high-order finite-difference code (OpenCFD-SC) is used to directly solve the full three-dimensional compressible Navier–Stokes equations for a perfect gas without any turbulence modeling. This code has been carefully validated and successfully adopted in previous DNS studies of a compression ramp[20] and reflected interactions.[21,22] The constitutive relation for a Newtonian fluid is used to calculate the viscous stress tensor σ_{ij}. The heat flux vector is computed according to Fourier's law of heat conduction, and the pressure p is related to the density ρ and the temperature T through the ideal gas state equation. Sutherland's law is used to determine the dynamic viscosity coefficient μ. The relation $k = \mu C_p/Pr$ is used to calculate the thermal conductivity, with the specific heat capacity ratio $\gamma = 1.4$ and the molecular Prandtl number $Pr = 0.71$. The specific heat capacity of the gas at constant pressure is taken as $C_p = \gamma R/(\gamma - 1)$, where R is the specific gas constant of air.

The inviscid fluxes in the governing equations are solved using the optimized fourth-order weighted essentially non-oscillatory (WENO) scheme introduced by Martin *et al.*[23] and the Steger–Warming splitting method. A set of optimal WENO weights is used in the linear part of this scheme, which maximizes the bandwidth-resolving efficiency. The numerical dissipation is further reduced by the combined use of absolute and relative limiters given by Wu and Martin.[24] The viscous fluxes are discretized by an eighth-order central difference scheme. A third-order explicit total variation diminishing Runge–Kutta method, proposed by Gottlieb and Shu,[25] is used to perform the time advancement. Detailed descriptions of the governing equations and the numerical methods are given by Tong *et al.*[20]

We use a grid consisting of $3127 \times 420 \times 340$ points in the x, y, and z directions, respectively, to discretize the computational domain. The grid spacing is uniform in the z-direction. A sketch of the computational grid in the x-y plane is shown in Fig. 2. In the x-direction, the well-resolved part of the domain is the interaction zone ranging from 50.8 to 90.2 mm, where 2627 points are equally distributed. In the transition zone $0 < x < 50.8$ mm and fringe zone $x > 90.2$ mm, 400 and 100 points are progressively refined and coarsened, respectively. In the y-direction, a hyperbolic tangent mapping is used, and the points are clustered toward the wall to increase the resolution of the turbulence scales in the near-wall region, where there are 280 points located inside the boundary layer. At x_{ref}, the grid spacings in wall units in the interaction zone are $\Delta x^+ = 8.5$ and $\Delta z^+ = 7.15$ in the streamwise and spanwise directions, respectively. The wall-normal spacing gradually increases from $\Delta y^+ = 0.55$ at the wall to $\Delta y^+ = 5.5$ at the edge of the upstream turbulent boundary layer. The present grid

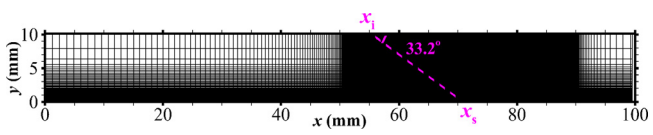

FIG. 2. A sketch of the computational grid in the x–y plane. The grid is plotted at intervals of ten and five points in the x and y directions, respectively. The pink dashed line denotes the impinging shock wave.

resolutions in the interaction zone are comparable to the previous well-accepted DNS of SWTBLIs by Priebe and Martin[15] and Fang *et al.*[18] Unless otherwise stated, the superscript "+" hereafter refers to a quantity in wall units at x_{ref}.

The boundary conditions applied in the simulation are now described. The domain is bounded by a steady laminar boundary layer profile at the inlet and supersonic outflow boundary conditions at the outlet. The laminar boundary layer profile is identical to the one used by Tong *et al.*,[11] who extracted it from an auxiliary flat plate simulation at the same inflow conditions. At the upper boundary of the domain, a no-reflecting boundary condition given by Poinsot and Lele[26] is enforced to eliminate disturbance reflections, and a jump in the flow variables obeying the Rankine–Hugoniot relations is directly imposed at $x_i = 55.6$ mm. At the bottom boundary, a no-slip isothermal boundary condition is applied. At the spanwise boundaries, periodic boundary conditions are enforced.

The unsteady wall-normal velocity disturbances in the blowing and suction region shown in Fig. 1 are the same as in the recent DNS of Tong *et al.*,[11] where the amplitude $A = 0.15U_\infty$ and the basic frequency $\varpi = 0.157\, U_\infty/\delta_0$ (δ_0 being the boundary layer thickness at the domain inlet) are set to generate fully developed turbulence upstream of the interaction. The profile of the laminar boundary layer at the inlet is used to initialize the three-dimensional flow field. Before collecting the flow samples, the simulation is performed for a time of $127\delta/U_\infty$ (equal to two flow-through times) to exclude the initial transient process completely. Once a statistically steady state is achieved, the simulation is then carried out for a longer time of $381\delta/U_\infty$ (six flow-through times). Statistical convergence is obtained by sampling 530 three-dimensional instantaneous flow fields at a constant time interval of $0.72\delta/U_\infty$, and the flow statistics are determined by taking the average of the three-dimensional flow fields in both time and the spanwise direction. A total of 3000 flow samples in the y–z plane at selected streamwise locations are collected at a constant time interval of $0.035\delta/U_\infty$ for the BEMD.

The fluctuating WHF signals throughout the interaction region are collected at a much shorter time interval of $0.014\delta/U_\infty$ to obtain fully time-resolved fluctuations, ensuring that the propagation and energy spectra of the WHF are accurately estimated. In the following results, bars and primes denote the average and fluctuating components using the standard Reynolds decomposition, whereas tildes and double-primes denote the density-weighted averages and fluctuating components using the Favre decomposition. Note that the velocities in the x, y, and z directions are represented by u, v, and w, respectively.

C. Validation

To validate the DNS data, we assess the spanwise two-point correlations of the velocity fluctuations in the interaction region to check the selected spanwise width. As suggested by Pirozzoli *et al.*,[17] the spanwise two-point correlation coefficient reported in Fig. 3 is defined as

$$R_{\alpha\alpha}(r_z) = \sum_{k=1}^{N_z-1} \overline{\alpha_k \alpha_{k+k_r}}, \tag{1}$$

where N_z and $r_z = k_r \Delta z$ denote the grid point number in the z-direction and the spanwise distance, respectively; $k_r = 0, 1, \ldots, k$, and α denote the velocity fluctuation. It can be seen from Fig. 3 that the

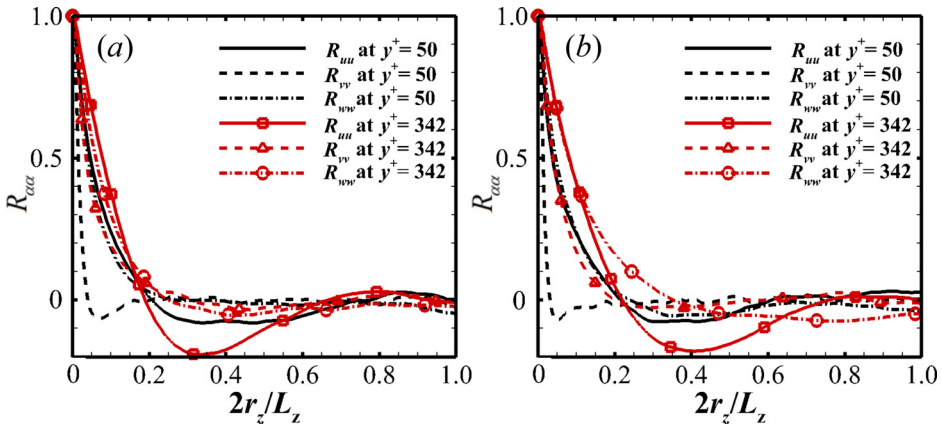

FIG. 3. Two-point correlations of the fluctuating velocity in the interaction: (a) $x = 70$ mm and (b) $x = 84$ mm.

correlation coefficients at $y^+ = 50$ and 342 rapidly decrease as the spanwise distance increases. The coefficients in the near-wall and outer regions are clearly near zero at spanwise distances close to $L_z/2$, confirming that turbulence fluctuations in the interaction are not inhibited, and the spanwise width of the computational domain is sufficient.

In Fig. 4, the van Driest transformed mean velocity profile at x_{ref} is compared with the DNS data of Fang *et al.*[18] and Tong *et al.*[27] for similar Mach and Reynolds numbers. Satisfactory agreement is observed, where a linear scaling is found for $y^+ < 6$ and a logarithmic scaling is present in the region $30 < y^+ < 100$. Next, the density-scaled Reynolds stress components plotted in Fig. 5 highlight close similarities with the experimental supersonic data of Elena and Lacharme[28] and the numerical results of Fang *et al.*,[18] Tong *et al.*,[27] and Pirozzoli *et al.*[29] In particular, the streamwise component attains a maximum value of 8.3 at $y^+ \approx 14$.

Moreover, it is seen from Fig. 6 that the production-to-dissipation ratio, defined as

$$P/\varepsilon = \frac{-\bar{\rho}^2 u_i'' u_j'' \partial \tilde{u}_i/\partial x_j}{\partial \sigma_{ij}'' u_i''/\partial x_j}, \tag{2}$$

shows reasonable agreement with the results of Sun *et al.*,[30] Tong *et al.*,[11] and Schlatter and Örlü.[31] This ratio peaks at $y^+ \approx 12$, attaining a maximum value of $P/\varepsilon \approx 1.9$ and relaxing toward a nearly constant level ($P/\varepsilon \approx 1.0$) for $40 < y^+ < 100$. These results ensure that the inflow turbulence generation method in the present simulation is reliable.

A grid-sensitivity study is performed to assess the chosen grid resolution, where the number of the grid points in the integration region is refined by 50% in both the x and z directions. The streamwise distributions of mean wall pressure $\bar{P}_w/P_\infty$, skin friction coefficient $\bar{C}_f$, and wall heat flux coefficient $\bar{C}_h$ for both grids are compared quantitatively in Fig. 7, as a function of the scaled interaction coordinate $x^* = (x - x_s)/\delta$. In the following, the wall heat flux C_h coefficient is defined as

$$C_h = \frac{k(\partial T/\partial y)_w}{\rho_\infty U_\infty C_p (T_w - T_r)}. \tag{3}$$

No significant changes in the interaction zone are observed, and the deviations are less than 5%. In particular, the streamwise locations of mean separation and reattachment points, corresponding to $\bar{C}_f = 0$ in Fig. 7(b), are only slightly changed. Therefore, it is confirmed that the present baseline grid is reasonably suitable.

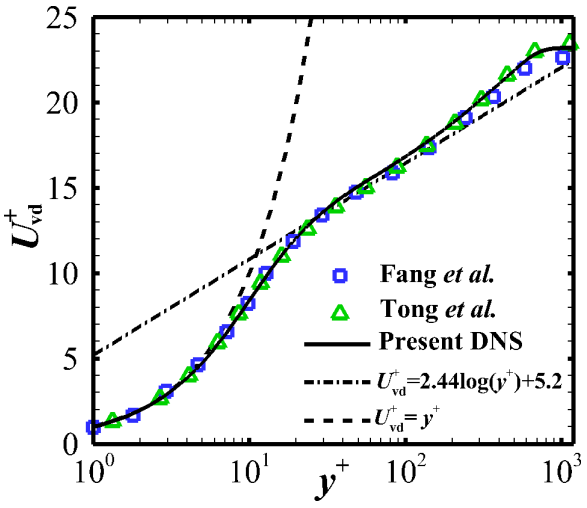

FIG. 4. Profile of the van Driest transformed mean velocity U_{vd}^+ at x_{ref}.

III. RESULTS AND DISCUSSION

A. Instantaneous and mean flow properties

Figure 8 shows iso-surfaces of the Q criterion[32] and the pressure gradient modulus to visualize the influence of the shock interaction on the coherent vortical structures. A small iso-surface threshold of $Q/Q_{max} = 0.005$ (Q_{max} being the maximum value of Q) is selected for better visualization, and this iso-surface is colored by the wall-normal distance. Consistent with the numerical observations of Priebe and Martin[15] and Fang *et al.*,[18] an augmentation of the turbulence structures is visually discernible after they pass through the interaction region. Unlike the elongated streaky structures dominating the near-wall region of the upstream boundary layer, large-scale streamwise vortical structures are apparent downstream of the interaction, mainly concentrated in the outer region of the reattached boundary layer.

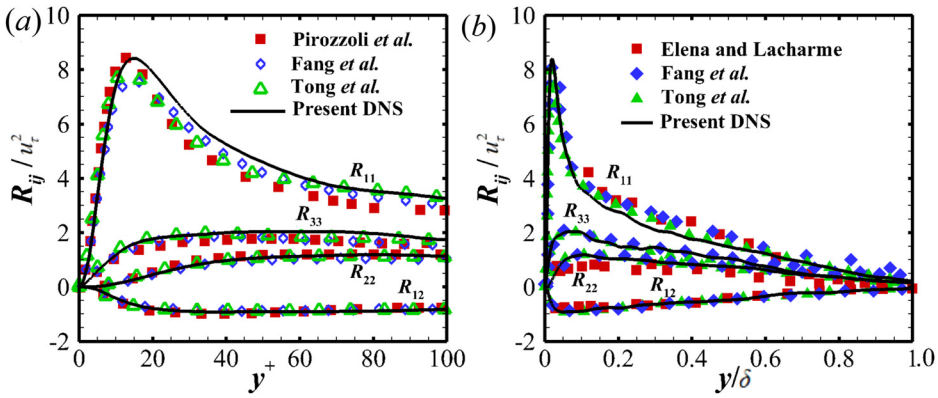

FIG. 5. Distributions of the density-scaled Reynolds stress components $R_{ij} = (\bar{\rho}/\bar{\rho}_w)u_i''u_j''$ at x_{ref}: (a) inner scaling and (b) outer scaling.

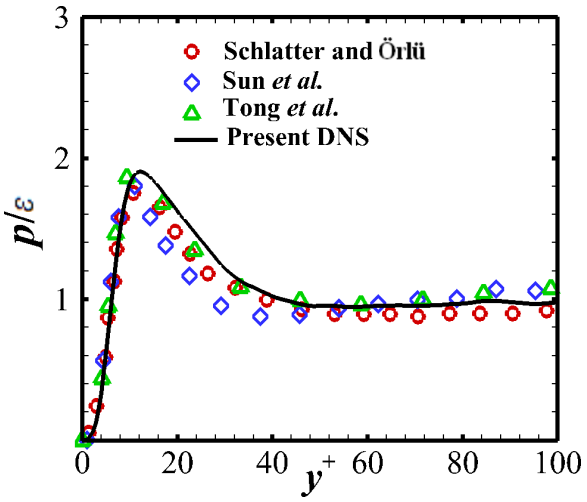

FIG. 6. Distribution of the production-to-dissipation rate P/ε at x_{ref}.

This behavior has previously been attributed to the formation and development of the separated shear layer, as suggested by Fang *et al.*[18] and Pirozzoli and Grasso.[33]

Figure 9 shows an instantaneous distribution of the fluctuating WFH C_h' in the interaction zone. Signatures of intense streaky structures are observed in the upstream boundary layer, implying the dominance of the streamwise coherence. These streaks are dramatically altered between the mean separation point S and reattachment point R, where the streamwise length scale is significantly reduced. A key observation in the downstream region is that the reoccurrence of the streaks with larger streamwise length scales is clear for $x^* > 4$. This trend is quantified in the following correlation analysis. Six streamwise locations over the interaction zone are selected to investigate the evolution of the fluctuating WHF. As labeled in Fig. 9, one point is located at x_{ref}, and two points are located at the mean separation and reattachment points, respectively. The other three points x_1–x_3 are placed in the downstream region.

To investigate the scaling linking the mean WHF to the mean skin friction, the Reynolds analogy factor, defined as Reynolds analogy factor (RAF) $= 2\bar{C}_h/\bar{C}_f$, is shown in Fig. 10(a) as a function of x^*. The RAF is nearly constant at about 1.1 upstream of the interaction.

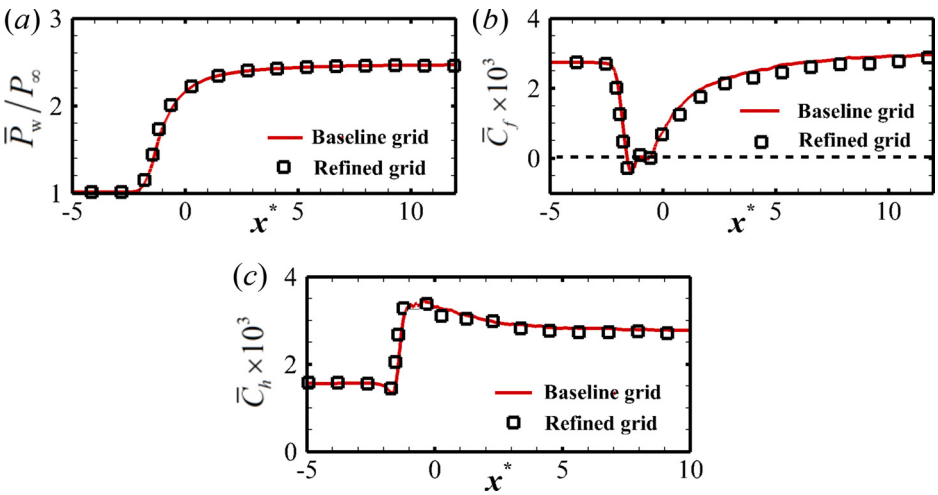

FIG. 7. Streamwise distributions of mean surface quantities: (a) pressure, (b) skin friction coefficient, and (c) WHF.

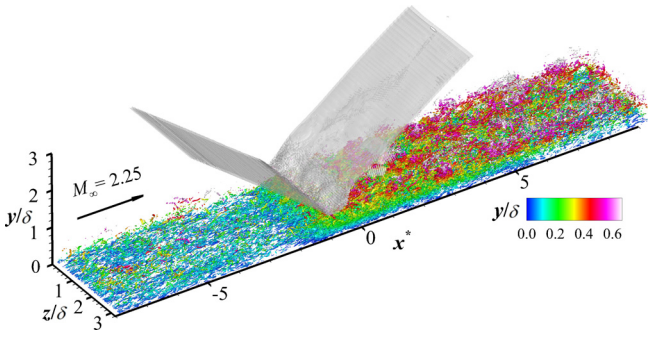

FIG. 8. Coherent vortical structures extracted using iso-surface of Q equal to 0.5% of its global maximum and are colored by the wall-normal distance. The shock system is visualized using the gray iso-surface of $|\nabla P|\delta/P_\infty = 150$.

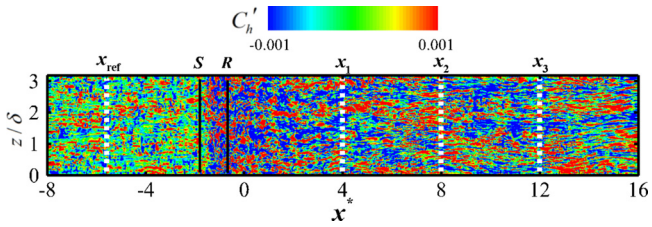

FIG. 9. Instantaneous flow field of the fluctuating WFH C_h'.

This value is close to 1.2, obtained in the DNS of a hypersonic turbulent boundary layer by Priebe and Martin.[34] In the separation region, this scaling is not valid because of the small negative $\bar{C}_f$ (see Fig. 7) at the location close to the mean separation and reattachment points. Starting at R, the downstream RAF exhibits a rapid drop, achieving a value of about 2.0 at $x^* = 12$. In Fig. 10(b), the streamwise distribution of the QP85 scaling,[4] defined as $\mathrm{QP85} = (\bar{C}_h/\bar{C}_o)(\bar{P}_o/\bar{P}_w)^{0.85}$, is reported to reveal the relation between the mean WHF and the mean wall pressure. The variables $\bar{C}_o$ and $\bar{P}_o$ denote the values of $\bar{C}_h$ and $\bar{P}_w$ upstream of the interaction. QP85 deviates somewhat from the scaling, varying between 0.8 and 1.37 in the separation region, and slowly approaches about 0.8 at $x^* = 12$. The results emphasize that the mean WHF scales better with the mean wall pressure than the mean skin friction, which confirms the validity of the QP85 scaling in a supersonic SWTBLI with separation.

B. Probability density function

Figure 11 shows the probability density function (PDF) of the normalized WHF C_h^+ at various streamwise locations. The PDFs are all positively skewed, peaking at about $C_h^+ = 0.7$, suggesting that the shock interaction exhibits little influence on the PDF shape. Remarkable differences are observed at the positive and negative PDF tails for locations S and R. Compared to the PDF at x_{ref}, both the tails at S become wider, indicating an increased occurrence probability of the extreme WHF and a relatively decreased skewness. At R, the positive tail becomes even larger, while the negative tail experiences a significant decrease, becoming lower than for x_{ref}. At x_1–x_3, the positive tails are slightly changed, approaching the upstream values, while the negative tails become narrower, indicating that the negative WHF occurs less frequently downstream of the interaction. It is reasonably inferred that the recovery of the positive WHF is much faster than that of the negative WHF in the reattached boundary layer.

Figure 12 shows the PDFs of the WHF fluctuations C_h' at different streamwise locations, where the normalization is with the local root-mean-squared (RMS) value C_{rms}. Apparently, all the PDFs are highly negatively skewed, with the peak located at about $C_h'/C_{rms} = -0.5$, which is in accordance with previous analysis of the PDFs of the wall shear stress fluctuations in the reflected interaction by Tong *et al.*[27] It is interesting to note that the normalized PDFs collapse well, except for the extremely negative tails ($C_h'/C_{rms} < -2$) at x_{ref}, S and R. This might be a reflection of the regenerated streaky structures in the downstream region (see Fig. 9). Another important finding is that the PDFs of the normalized WHF fluctuations are in good agreement with the PDFs of the wall shear stress fluctuations in the low-speed experiments of Grosse and Schröder,[35] Nottebrock *et al.*,[36] and Sreenivasan and Antonia[37] at different Reynolds numbers.

C. Spectral analysis

The pre-multiplied spectra of the wall pressure and WHF fluctuations at the six streamwise locations are reported in Figs. 13 and 14, respectively, as a function of the normalized frequency $f\delta/U_\infty$, where $\Phi(f)$ is the power spectral density (PSD) of the fluctuations. The overall fluctuating signal at each location is decomposed into six segments

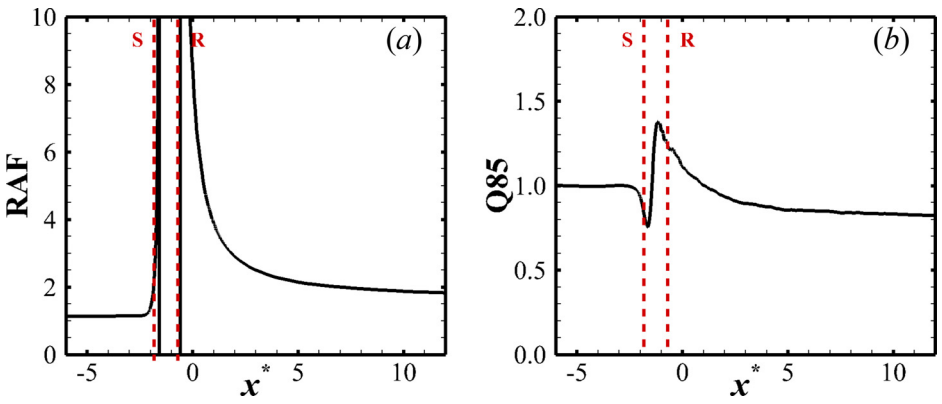

FIG. 10. Streamwise distributions of (a) Reynolds analogy factor and (b) QP85 scaling.

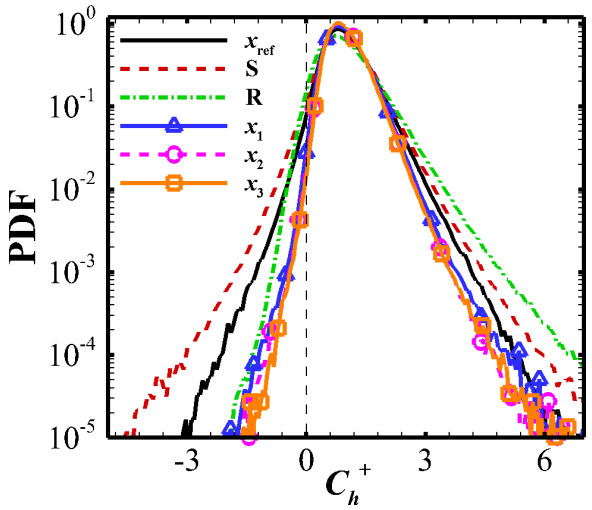

FIG. 11. Probability density function of the WHF normalized by the local mean values.

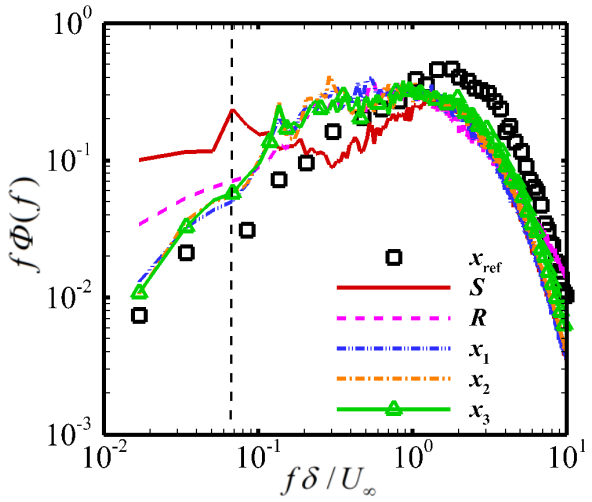

FIG. 13. Pre-multiplied spectra of wall pressure fluctuations at different streamwise locations.

with 50% overlap, and the PSD is estimated using Welch's algorithm with a Hamming window. The spanwise-averaged spectra are normalized with the square of the RMS value of the fluctuations.

In Fig. 13, the wall pressure fluctuation spectra throughout the interaction region confirm the existence of low-frequency unsteadiness, which has often been mentioned in previous numerical and experimental studies of SWTBLI flows. At x_{ref}, a broadband peak centering at about $f\delta/U_\infty \approx O(1)$ is dominant, indicative of energetic turbulent structures in the upstream undisturbed boundary layer. It is apparent from the spectra at the mean separation point S that the low-frequency energy is significantly enhanced, with a peak located at $f\delta/U_\infty = 0.07$. This behavior clearly reflects the low-frequency motion of the separated shock wave in the interaction. At locations further downstream, the low-frequency energy rapidly decreases as expected. At x_1–x_3, most of the energy is characterized by intermediate to high frequencies because of the reattached boundary layer thickening.

A completely different scenario in the spectra of the fluctuating WHF is observed in Fig. 14. It is highlighted that the effect of the unsteady shock motion exhibits little influence on the low-frequency energy. Compared to x_{ref}, the shape of the spectra at S changes only slightly. It is noted that no enhancement of the low-frequency component is found, and most of the energy is still present at high frequencies $f\delta/U_\infty > 1.0$. The figure also shows that the spectra at R and x_1–x_3 are modulated by the upstream shock waves. The high-frequency components are significantly attenuated, while the component in the intermediate frequency range is strongly enhanced. These changes

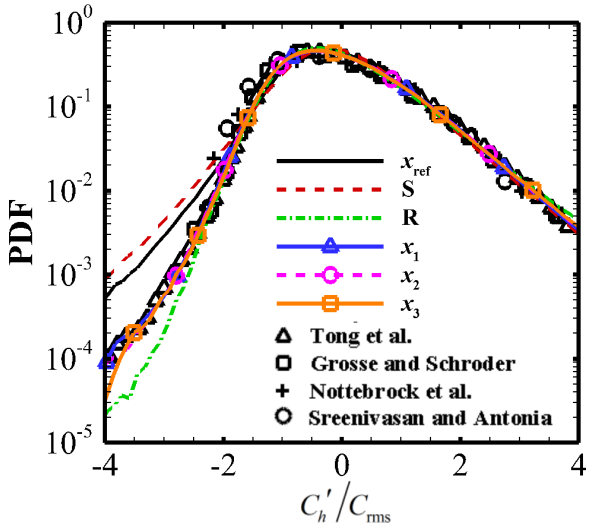

FIG. 12. Probability density function of the WHF fluctuation C_h' normalized by the local RMS value C_{rms}.

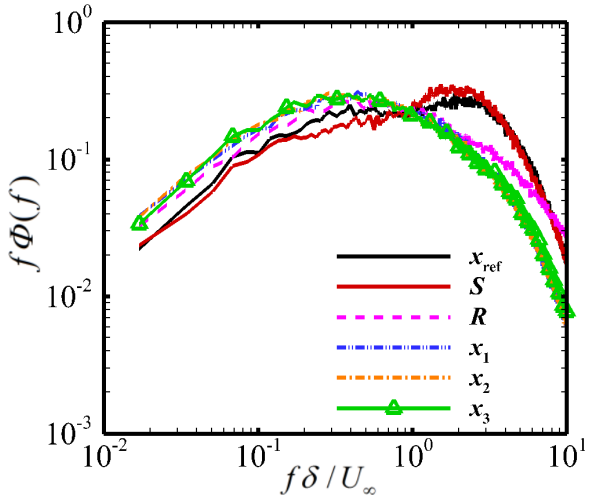

FIG. 14. Pre-multiplied spectra of the fluctuating WHF at different streamwise locations.

result in a broadband peak between $f\delta/U_\infty = 0.1$ and 1.0. This trend is different from the recent DNS study of Volpiani *et al.*[16] They analyzed the WHF spectra in SWTBLI under similar flow conditions and shock strength and stated that a shift toward intermediate frequencies was not observed in their cooled case. This difference is probably linked to the wall cooling effect. In the DNS of Volpiani *et al.*,[16] $T_w/T_r = 0.5$, which is lower than the value $T_w/T_r = 0.75$ used in the present study.

The effect of the shock motion on the energy distribution in a particular frequency range is quantified by integrating the PSD, as shown in Fig. 15. Following Fang *et al.*,[18] the integration for a given frequency f is defined as

$$\Gamma = \int_0^f \Phi(\zeta) d\zeta. \tag{4}$$

Here, the overall frequency range is divided into three zones, $f\delta/U_\infty \leq 0.1$, $0.1 < f\delta/U_\infty < 1.0$, and $f\delta/U_\infty \geq 1.0$, which correspond to low-, intermediate-, and high-frequency components, respectively. The low-frequency energy in the wall pressure spectra at x_{ref} is only 4% but increases to 33% at S. For the WHF, the portions at x_{ref} and S are 14% and 13%, respectively, confirming that the fluctuating WHF is weakly related to the low-frequency unsteady shock motion. Moreover, the portion of the high-frequency components in the WHF spectra decreases from 42% at x_{ref} to 22% at x_1–x_3. By contrast, the intermediate frequency contribution increases from 44% to 58%, supporting the dominance of the intermediate frequency components in the spectra of the fluctuating WHF downstream of the interaction.

D. Space–time correlations

The two-point space–time correlation coefficients R_{cc} (Δx^+, Δz^+, Δt^+) at six streamwise locations are comparatively investigated to shed some light on the spatial and temporal properties of the fluctuating WHF field. The coefficient R_{cc} is defined as

$$R_{cc} = \frac{\overline{C_h'(x_0, z, t) C_h'(x_0 + \Delta x^+, z + \Delta z^+, t + \Delta t^+)}}{\sqrt{\overline{C_h'(x_0, z, t)^2}} \sqrt{\overline{C_h'(x_0 + \Delta x^+, z + \Delta z^+, t + \Delta t^+)^2}}}, \tag{5}$$

where the spatial separations in the x- and z-directions are denoted by Δx^+ and Δz^+, respectively, and Δt^+ is the time delay. The reference probe is denoted by x_o.

Figure 16 shows maps of the two-point spatial correlation R_{cc} (Δx^+, Δz^+, 0). Note that the axes in the different correlation maps do not use the same scales for better visualization. At x_{ref}, the correlation map in Fig. 16(a) is characterized by an elongated streamwise distribution, reflecting the streaky structures observed in the upstream turbulent boundary layer. Two interesting observations regarding the variations of the correlation maps throughout the interaction region are identified. First, at S and R, the spatial extent in the streamwise direction significantly decreases, whereas the extent in the spanwise direction slightly increases, indicating decreased anisotropy in the separation region. This scenario can be better observed from Fig. 16(c) in which the correlation map at R is roughly circular. Taking the correlation level of 0.3 as an example, the streamwise and spanwise extents are $\Delta x^+ = 90$ and $\Delta z^+ = 80$, respectively, compared to $\Delta x^+ = 216$ and $\Delta z^+ = 68$ at x_{ref}. The reason for the reduced anisotropy in the separation region is likely the destruction of the spanwise-alternating stripes of the WHF fluctuations due to the existence of the separated flows. The present DNS results are different from the observations of the two-point correlation maps of wall shear stress fluctuations provided by Tong *et al.*[27] in a supersonic separated SWTBLI. In their data, the highly spanwise elongated contour shape is a consequence of the noted increase in the spanwise coherence and the significant decrease in the streamwise coherence. It is suggested that the fluctuating WHF is nearly isotropic in the separation region. Second, at x_1–x_3, we observe that the spatial extent of the correlation maps exhibits a significant increase in the streamwise direction and a slight decrease in the spanwise direction. As a result, the maps become elongated in the streamwise direction again, corresponding to the regeneration of the streaky structures downstream of $x^* = 4$. For instance, the extent in the streamwise and spanwise direction is about $\Delta x^+ = 298$ and $\Delta z^+ = 50$ for a correlation value of 0.3 in Fig. 16(f). This shows that the regenerated streaks have larger streamwise correlation lengths, as previously mentioned in Fig. 9, suggesting that the recovery of the spanwise-alternating streaky structure is not fully completed. Furthermore, it is interesting to notice that the present two-point correlation analysis resembles very closely the wall shear stress correlations downstream of the interaction performed by Tong *et al.*[27] in the reflected interaction.

Figure 17 shows maps of the space–time correlation coefficient R_{cc} (Δx^+, 0, Δt^+) at the six streamwise locations. The convective nature of the WHF fluctuations in the present study is in good

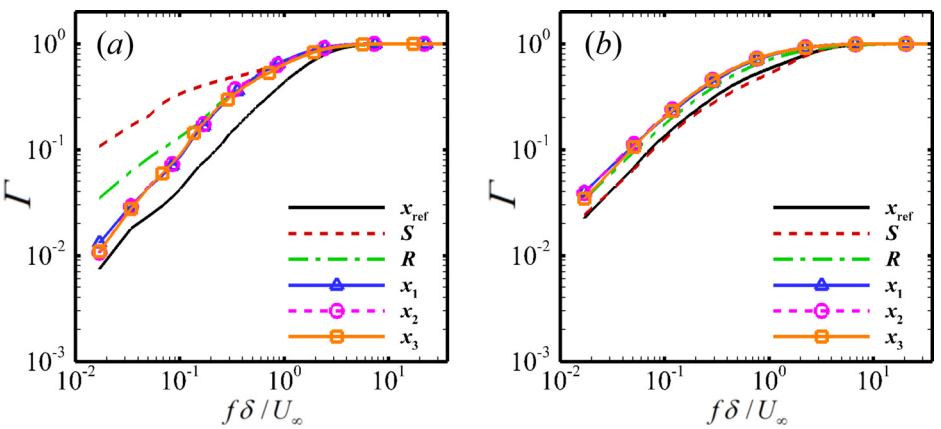

FIG. 15. Integrations of (a) wall pressure and (b) WHF spectra at different streamwise locations.

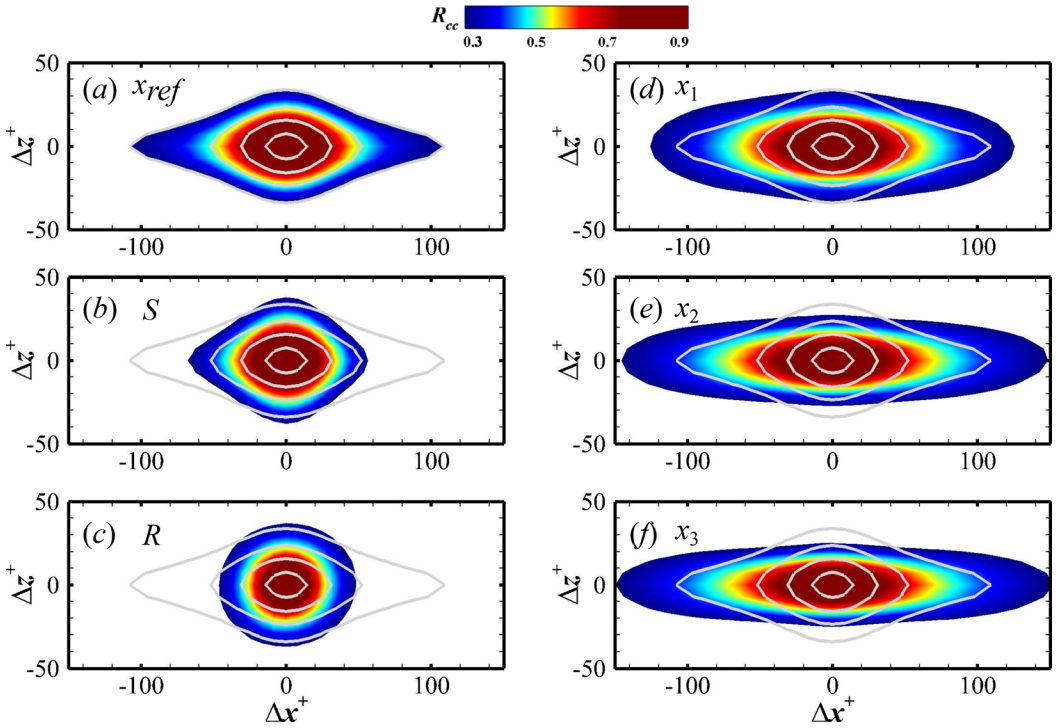

FIG. 16. Contours of the two-point correlation coefficients for $\Delta t^+ = 0$ at (a) x_{ref}, (b) S, (c) R, (d) x_1, (e) x_2, and (f) x_3 with values below 0.3 omitted. The gray iso-lines denote the results at x_{ref}, corresponding to four levels between 0.3 and 0.9 with an increment of 0.2.

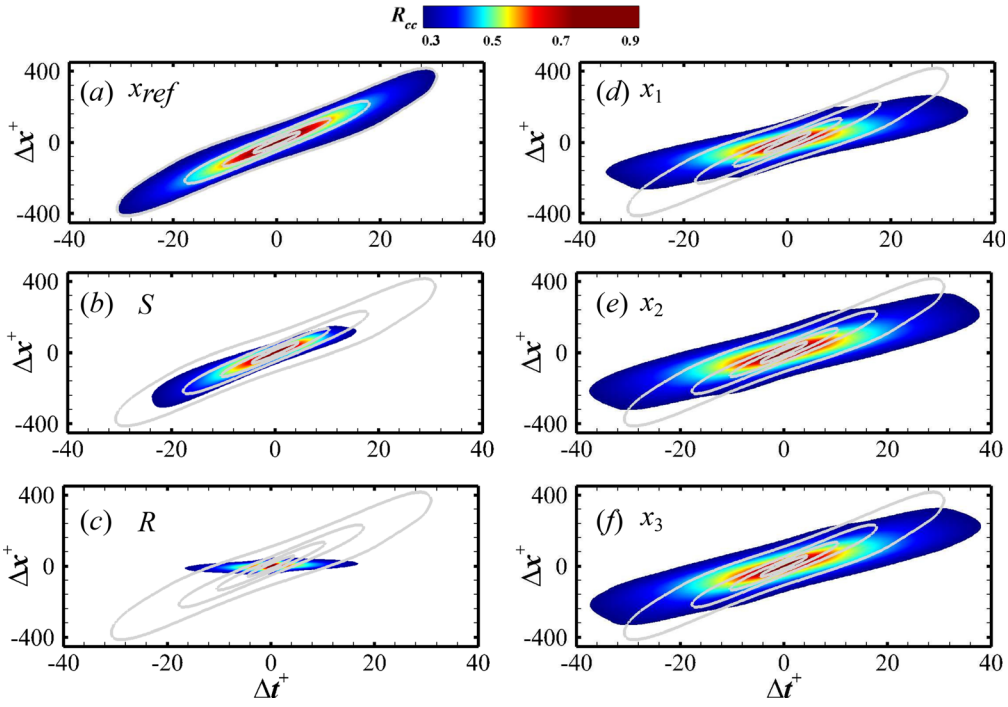

FIG. 17. Contours of the space–time correlation coefficients for $\Delta z^+ = 0$ at (a) x_{ref}, (b) S, (c) R, (d) x_1, (e) x_2, and (f) x_3 with values below 0.3 omitted. The gray iso-lines denote the results at x_{ref}, corresponding to four levels between 0.3 and 0.9 with an increment of 0.2.

agreement with the wall pressure field correlations in a transonic shock/boundary layer interaction by Bernardini *et al.*[38] All the maps in Fig. 17 are highly skewed and characterized by a narrow forward-leaning elliptical behavior, where the major axes are inclined in the first and third quadrant of the Δt^+–Δz^+ plane. This means that the downstream propagation of the WHF fluctuations is generally maintained in the interaction region. However, the spatial and temporal extents of the correlation maps at S and R experience a systematic reduction, leading to a sharp contraction observed in Figs. 17(b) and 17(c). It is suggested that the spatial and temporal coherence of the fluctuating WHF is significantly reduced in the separation region, very similar to the space–time correlation analysis of the wall shear stress field reported by Tong *et al.*[27] At x_1–x_3, a rapid recovery is identified in Figs. 17(d)–17(f). Specifically, the temporal extent for the 0.3 correlation level at location R decreases to about 50% of the upstream value, whereas the temporal extent at x_3 increases by about 1.2 times. Another striking feature is the variation in the inclination of the correlation map. The inclination angle of the major axis with respect to the delay time axis experiences a monotonic decrease at S and R, followed by a rapid increase at x_1–x_3. In Fig. 17(f), it is apparent that the angle at x_3 is still lower than that at x_{ref}, further indicating that the spatial and temporal evolution of the fluctuating WHF field has not fully recovered in the downstream region.

Differences can be better understood by comparing the convection velocity U_c reported in Fig. 18. Similar to Duan *et al.*,[39] the convection velocity for a given time delay Δt^+ is computed as the ratio $\Delta x^+/\Delta t^+$ with Δx^+ corresponding to the value where

$$\left.\frac{\partial R_{cc}(r_x, 0, \Delta t^+)}{\partial r_x}\right|_{r_x=\Delta x^+} = 0. \tag{6}$$

As seen in Fig. 18, the computed convective velocity depends weakly on the time delay Δt^+. At x_{ref}, the fluctuating WHF propagates downstream at about $U_c = 0.55U_\infty$–$0.62U_\infty$. The convection velocity monotonically decreases at S and R, dropping to $0.37U_\infty$–$0.43U_\infty$ and $0.04U_\infty$–$0.1U_\infty$, respectively. The significant reduction in the convection velocity is probably linked to the reversed flow structures in the separation region. At x_1–x_3, the convection velocity persistently increases but still smaller than that at x_{ref}, varying between $0.2U_\infty$ and $0.4U_\infty$, confirming that the recovery process is incomplete.

E. Decomposition of mean WHF

As suggested by Sun *et al.*,[10] the decomposition of the mean WHF $\bar{C}_h$ for compressible boundary layer flows is derived from the integration of the total energy equation from the wall to the free stream, expressed as

$$\begin{aligned}\bar{C}_h = &\underbrace{\frac{1}{\rho_\infty U_\infty^4}\int_0^\infty k\frac{\partial \bar{T}}{\partial y}\frac{\partial \tilde{u}}{\partial y}dy}_{C_{h,\mathrm{C}}} + \underbrace{\frac{1}{\rho_\infty U_\infty^4}\int_0^\infty -c_p\bar{\rho}\nu''T''\frac{\partial \tilde{u}}{\partial y}dy}_{C_{h,\mathrm{TH}}} + \underbrace{\frac{1}{\rho_\infty U_\infty^4}\int_0^\infty \overline{u_k''\sigma_{kj}}\frac{\partial \tilde{u}}{\partial y}dy}_{C_{h,\mathrm{MD}}} + \underbrace{\frac{1}{\rho_\infty U_\infty^4}\int_0^\infty -\frac{1}{2}\overline{\rho u_k''u_k''u_j''}\frac{\partial \tilde{u}}{\partial y}dy}_{C_{h,\mathrm{TKE}}}\\
&+ \underbrace{\frac{1}{\rho_\infty U_\infty^4}\int_0^\infty \tilde{u}_k\sigma_{kj}\frac{\partial \tilde{u}}{\partial y}dy}_{C_{h,\mathrm{MS}}} + \underbrace{\frac{1}{\rho_\infty U_\infty^4}\int_0^\infty -\tilde{u}_k\bar{\rho}u_k''u_j''\frac{\partial \tilde{u}}{\partial y}dy}_{C_{h,RS}} + \underbrace{\frac{1}{\rho_\infty U_\infty^4}\int_0^\infty (\tilde{u}-U_\infty)\left(\bar{\rho}\frac{D\tilde{E}}{Dt}\right)dy}_{C_{h,\mathrm{G1}}} + \underbrace{\frac{1}{\rho_\infty U_\infty^4}\int_0^\infty (\tilde{u}-U_\infty)\left[\frac{\partial(\bar{u}\bar{p})}{\partial x}+\frac{\partial(\bar{v}\bar{p})}{\partial y}\right]dy}_{C_{h,\mathrm{G2}}}\\
&+ \underbrace{\frac{1}{\rho_\infty U_\infty^4}\int_0^\infty (\tilde{u}-U_\infty)\left(k\frac{\partial \bar{T}}{\partial x} - c_p\bar{\rho}u''T'' + \overline{u_k''\sigma_{ki}} - \frac{1}{2}\overline{\rho u_k''u_k''u_i''} + \tilde{u}_k\sigma_{kj} - \tilde{u}_k\overline{\rho u_k''u_i''}\right)dy}_{C_{h,\mathrm{G3}}},\end{aligned} \tag{7}$$

where $C_{h,\mathrm{C}}$, $C_{h,\mathrm{TH}}$, $C_{h,\mathrm{MD}}$, $C_{h,\mathrm{TKE}}$, $C_{h,\mathrm{MS}}$, and $C_{h,\mathrm{RS}}$, respectively, represent the contributions of heat conduction, turbulent heat transport, the wall-normal component of the molecular diffusion, transport of turbulence kinetic energy (TKE), the work of the molecular stresses, and the Reynolds stresses. The terms $C_{h,\mathrm{G1}}$, $C_{h,\mathrm{G2}}$, and $C_{h,\mathrm{G3}}$ account for the temporal variation of the specific total energy E, pressure work, and the streamwise heterogeneity, respectively.

In a previous paper, the authors performed a scale-based decomposition analysis of the mean WHF generation in a zero-pressure-gradient spatially developing supersonic turbulent boundary layer under the same flow conditions.[11] It was found that the small-scale structures in the inner region carried a significant positive contribution to the mean WHF generation, whereas the large-scale structures in the logarithmic and outer regions were dominant, transporting the excess heat away from the wall. In this section, we numerically investigate the mean WHF generation downstream of the interaction through a direct comparison of the decomposed results in the previous decomposition of the value in the upstream turbulent boundary layer.[11] The above decomposition of the mean WHF is applied in SWTBLI for the first time to the author's knowledge, which provides comparative information on the quantitative contribution of coherent turbulent structures with specific length scales to the generation of the mean WHF throughout the interaction. Recalling that the mean WHF distribution reported in Fig. 7(c) experiences strong amplification in the interaction zone and nearly plateaus at $x^* > 4$, only the decomposition of $\bar{C}_h$ at $x^* = 10$ is shown for a better comparison. Note that no significant change is observed at other locations at $x^* > 4$, which are not shown here for brevity.

Figure 19 shows the decomposition of $\bar{C}_h$. The relative error, defined as $(C_{h,\mathrm{SUM}}-C_{h,\mathrm{DNS}})/C_{h,\mathrm{DNS}}$, is estimated at 0.12%, where $C_{h,\mathrm{SUM}}$ and $C_{h,\mathrm{DNS}}$ are the sum of the nine decomposed components and the mean WHF calculated using the raw DNS data, respectively. This suggests that the present decomposition is highly reliable. The mean WHF generation is dominated by the positive $C_{h,\mathrm{RS}}$ and negative $C_{h,\mathrm{TH}}$ values,

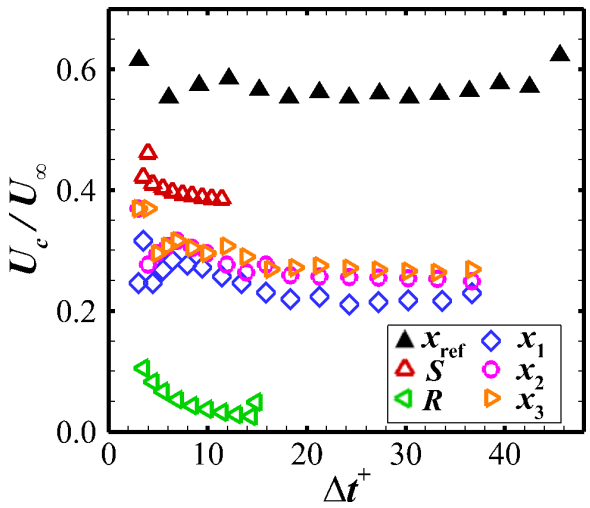

FIG. 18. Convection velocity at different streamwise locations.

reaching approximately 130.05% and –74.50%, respectively, whereas the contributions of the other components are relatively small and can be neglected in comparison. The general trend is consistent with the present authors' previous findings for an undisturbed turbulent boundary layer, where the positive contribution of $C_{h,\mathrm{RS}}$ and negative contribution of $C_{h,\mathrm{TH}}$ were about 126.67% and –76.64%, respectively. A notable difference is that the positive contribution of the molecular stresses $C_{h,\mathrm{M}}$ has a negligible value, about 16.37%, compared to 44.21% in the previous analysis of the undisturbed boundary layer. Considering the large positive $C_{h,\mathrm{RS}}$ (even larger than C_h) and the large negative $C_{h,\mathrm{TH}}$, it is apparent that the mean WHF generation in the downstream region features a counteraction between $C_{h,\mathrm{RS}}$ and $C_{h,\mathrm{TH}}$. The negative turbulent transport $C_{h,\mathrm{TH}}$ moves the excess heat at the wall generated by the work of the Reynolds stresses $C_{h,\mathrm{RS}}$ toward the outer region.

Following Cheng *et al.*,[40] the contributions of $C_{h,\mathrm{RS}}$ and $C_{h,\mathrm{TH}}$ are further investigated by decomposition using the BEMD method to quantify the contribution of turbulent structures associated with specific spanwise length scales. The wall-normal heat flux and Reynolds shear stress in Eq. (4) are rewritten as

$$\begin{aligned} -v''T'' &= -\sum_{i=1}^{4} v_i'' T_i'' - \sum_{i=1,j=1,i\neq j}^{4} v_i'' T_j'', \\ -u''v'' &= -\sum_{i=1}^{4} u_i'' v_i'' - \sum_{i=1,j=1,i\neq j}^{4} u_i'' v_j'', \end{aligned} \tag{8}$$

where u_i, v_i, and T_i, $i = 1, 2, 3, 4$, represent the velocity and temperature fluctuations corresponding to the four BEMD modes characterized by increasing spanwise length scales. Thus, the wall-normal heat flux and Reynolds shear stress are split into four diagonal and 12 non-diagonal terms. Subsequently, $C_{h,\mathrm{RS}}$ and $C_{h,\mathrm{TH}}$ are further split into the corresponding 16 terms, denoted by the mode number index (i, j) with i and j being the ith and jth BEMD mode and expressed as

$$C_{h,TH} = \underbrace{\frac{1}{\rho_\infty U_\infty^4}\int_0^\infty -c_p\bar{\rho}v_1''T_1''\frac{\partial\tilde{u}}{\partial y}dy}_{(1,1)} + \underbrace{\frac{1}{\rho_\infty U_\infty^4}\int_0^\infty -c_p\bar{\rho}v_1''T_2''\frac{\partial\tilde{u}}{\partial y}dy}_{(1,2)} + \cdots + \underbrace{\frac{1}{\rho_\infty U_\infty^4}\int_0^\infty -c_p\bar{\rho}v_4''T_4''\frac{\partial\tilde{u}}{\partial y}dy}_{(4,4)}, \tag{9}$$

$$C_{h,\mathrm{RS}} = \underbrace{\frac{1}{\rho_\infty U_\infty^4}\int_0^\infty -\tilde{u}\bar{\rho}u_1''v_1''\frac{\partial\tilde{u}}{\partial y}dy}_{(1,1)} + \underbrace{\frac{1}{\rho_\infty U_\infty^4}\int_0^\infty -\tilde{u}\bar{\rho}u_1''v_2''\frac{\partial\tilde{u}}{\partial y}dy}_{(1,2)} + \cdots + \underbrace{\frac{1}{\rho_\infty U_\infty^4}\int_0^\infty -\tilde{u}\bar{\rho}u_4''v_4''\frac{\partial\tilde{u}}{\partial y}dy}_{(4,4)}. \tag{10}$$

Here, the four diagonal components, (1, 1), (2, 2), (3, 3), and (4, 4) account for the contributions related to turbulent fluctuations with specific spanwise length scales, whereas the other 12 non-diagonal components represent the contributions from the interactions between different spanwise scales. Under such decomposition, the component (1, 1) is mainly produced by small-scale structures in the near-wall region, and the component (4, 4) is associated with large-scale structures in the outer region. The contributions generated by intermediate-scale structures are denoted by the components (2, 2) and (3, 3). Note that the components related to the Reynolds shear

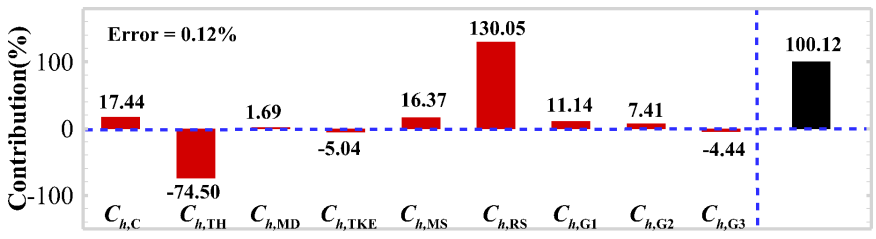

FIG. 19. Decomposition of the mean WHF at $x^* = 10$. The sum of the components is denoted by the black bar.

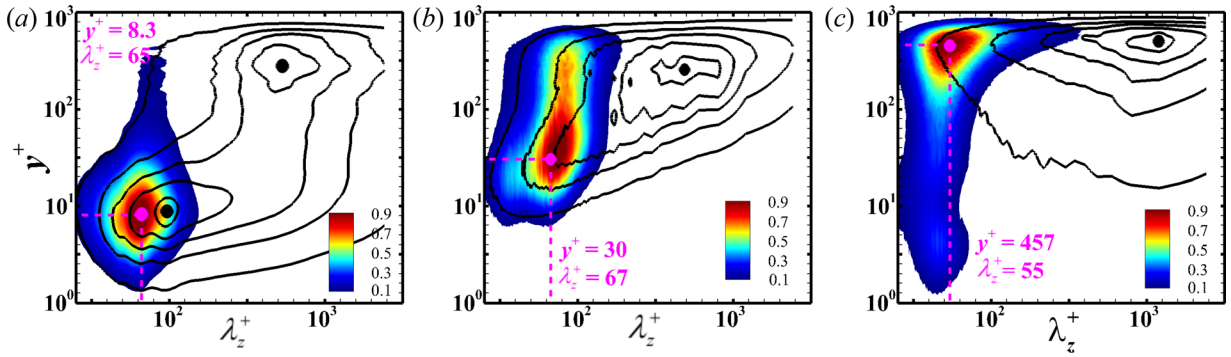

FIG. 20. Pre-multiplied spanwise spectra of the decomposed fluctuations in the first mode with values below 0.1 omitted: (a) u, (b) v, and (c) T. The spectra are normalized by the maximum value. The original spectra for the raw DNS data are denoted by five equally spaced iso-lines, from 0.1 to 0.9. The black and pink circles represent the spectral peaks for the raw DNS data and first BEMD mode, respectively.

stress contribute almost 95% of $C_{h,\mathrm{RS}}$, so the other components of $C_{h,\mathrm{RS}}$ are neglected in the above decomposition because of their relatively smaller magnitudes.

In Figs. 20–23, the pre-multiplied spanwise spectra of u'', v'', and T'' for the four modes are compared with the full spectra. For u'', the original spectra are dominated by two peaks, one inner peak at ($y^+ = 8.7$, $\lambda_z^+ = 95$) and one outer peak at ($y^+ = 281.8$, $\lambda_z^+ = 525$). This is different from the previous findings of the upstream turbulent boundary layer, where the spectra are characterized by an inner peak centering at $y^+ = 130$ and $\lambda_z^+ = 120$, with no evident energy peak in the outer region. For v'' and T'', the original spectra are characterized by one outer peak each, located at ($y^+ = 251.2$, $\lambda_z^+ = 479$) and ($y^+ = 501.2$, $\lambda_z^+ = 1175$), respectively. Compared to an earlier study of the upstream turbulent boundary layer, the peak locations are moved outward and the energetic wavelengths are significantly increased, which is indicative of the great dominance of the outer large-scale velocity and temperature fluctuations in the downstream region.

As expected, the spectra of the decomposed fluctuations indicate that the characteristic spanwise wavelength becomes larger with increasing mode number. Specifically, the first mode spectra for u'', shown in Fig. 20(a), are concentrated in the small (y^+, λ_z^+) domain, with the peak appearing at ($y^+ = 8.3$, $\lambda_z^+ = 65$). This is a clear reflection of the regenerated near-wall streaky structures in the downstream region, as frequently observed in previous numerical studies of SWTBLIs. As shown in Fig. 23(a), the peak in the fourth-mode spectra appears at $\lambda_z^+ = 660$ ($\lambda_z = 0.86\delta$) and $y^+ = 272.9$, which is the symptom of large-scale outer structures dominating the downstream region. Similar large-scale structures were also reported in the reflected interactions of Pasquariello *et al.*[19] and Zhuang *et al.*,[41] who highlighted the existence of the often-discussed Görtler-type vortices characterized by a spanwise length scale of approximately δ. For the second and third modes of u'', it is seen that the spectra in Figs. 21(a) and 22(a) are characterized by intermediate-scale structures, with the energy peaks occurring at ($y^+ = 13.7$, $\lambda_z^+ = 154$) and ($y^+ = 20.3$, $\lambda_z^+ = 298$), respectively. In this sense, the overall trend of the original spectra is effectively captured by the selected four BEMD modes. Moreover, it is notable that the peak locations in the u'' and v'' spectra consistently move outward with increasing mode number, which is completely different from the decomposed spectra of T''. Interestingly, the spectra for the four modes reported in Figs. 20(c), 21(c), 22(c), and 23(c) are peaked at an approximately constant outer location, ranging between $\lambda_z^+ = 457$ and $\lambda_z^+ = 479$. Although the reason for this difference is unclear, it might be partially ascribed to the slower recovery of the near-wall region temperature streaks and a predominance of downstream large-scale temperature fluctuations. This could occur because the original T'' spectra are primarily centered in the large (y^+, λ_z^+) domain compared with the u'' and v'' spectra.

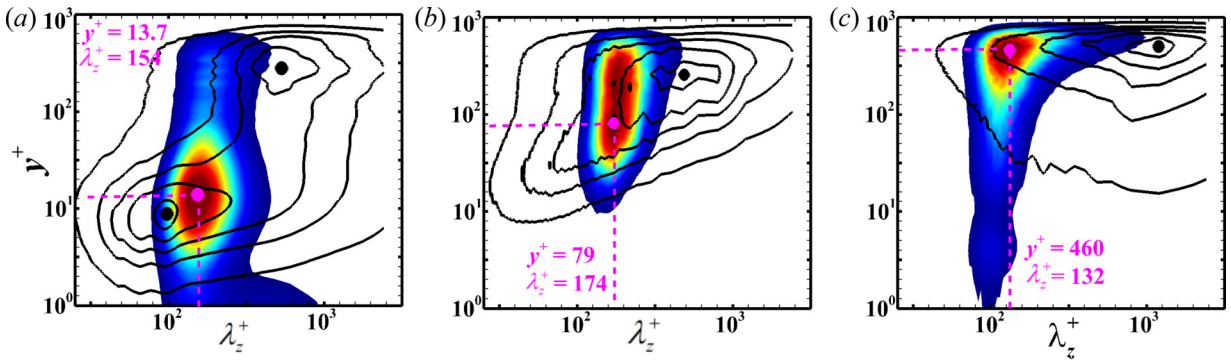

FIG. 21. Pre-multiplied spanwise spectra of the decomposed fluctuations in the second mode with values below 0.1 omitted: (a) u, (b) v, and (c) T. See Fig. 20 for the legend.

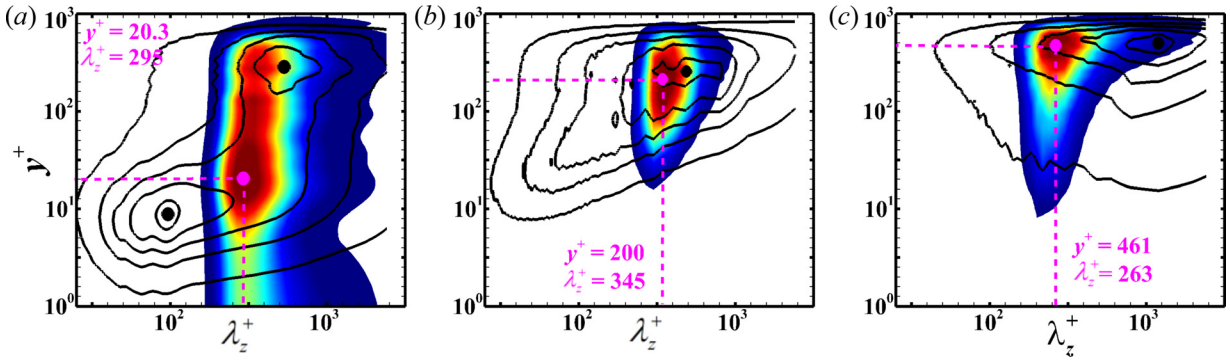

FIG. 22. Pre-multiplied spanwise spectra of the decomposed fluctuations in the third mode with values below 0.1 omitted: (a) *u*, (b) *v*, and (c) *T*. See Fig. 20 for the legend.

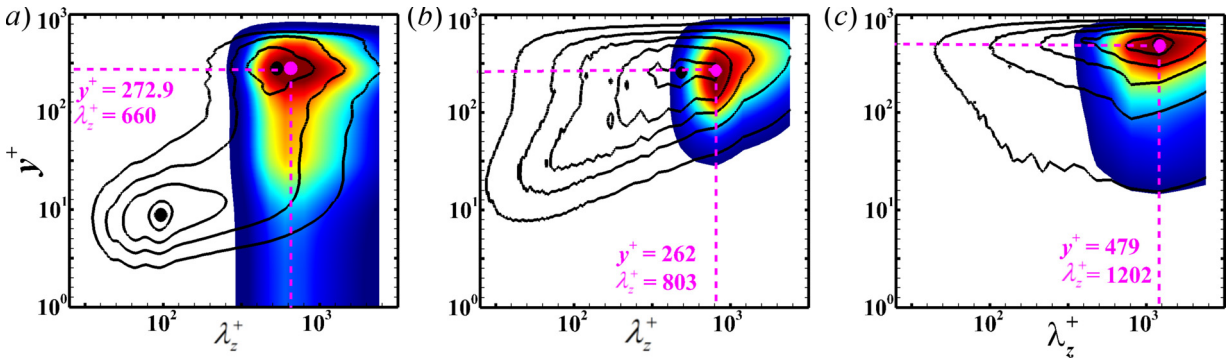

FIG. 23. Pre-multiplied spanwise spectra of the decomposed fluctuations in the fourth mode with values below 0.1 omitted: (a) *u*, (b) *v*, and (c) *T*. See Fig. 20 for the legend.

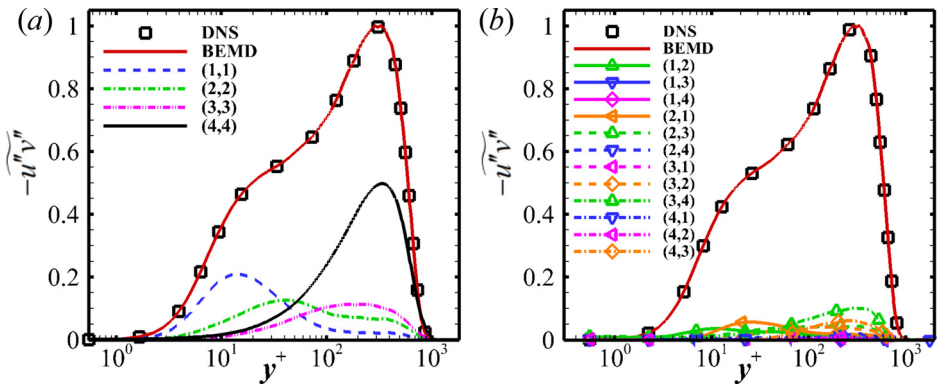

FIG. 24. Profiles of the decomposed Reynolds shear stress normalized by the maximum raw Reynolds shear stress: (a) diagonal components and (b) non-diagonal components.

A comparison of the 16 decomposed components with the complete Reynolds shear stress calculated using the raw DNS data is shown in Fig. 24 against y^+. Excellent collapse on the complete profile of the Reynolds shear stress is obtained for the sum of the 16 terms, which is a further confirmation of the accuracy of the present BEMD method. It is seen that the Reynolds shear stress generation is mainly dominated by the four diagonal components plotted in Fig. 24(a), while the contributions of the other 12 non-diagonal components reported in Fig. 24(b) are negligible. With respect to the four diagonal components, their profiles show a quite different scenario, where the diagonal component (4, 4) becomes dominant, suggesting that the complete Reynolds shear stress downstream of the interaction is characterized by the large-scale structures of u'' and v'' in the outer region. To be more specific, the shape of the diagonal component (4, 4) is similar to

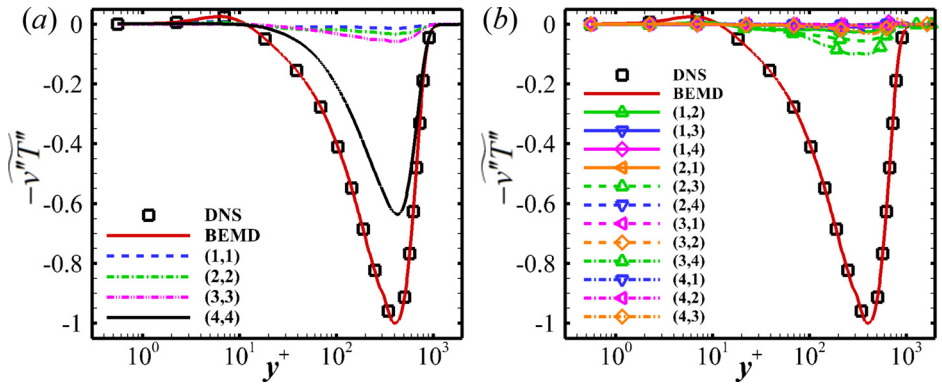

FIG. 25. Profiles of the decomposed wall-normal heat flux normalized by the maximum value of the raw wall-normal heat flux: (a) diagonal components and (b) non-diagonal components.

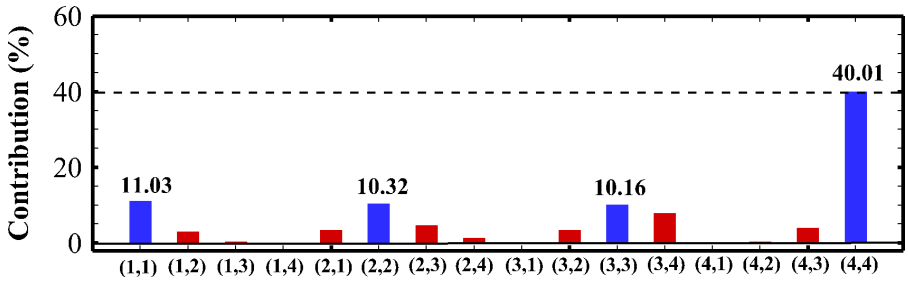

FIG. 26. Decomposition of $C_{h,\mathrm{RS}}$. The diagonal and non-diagonal components are denoted by the blue and red bars, respectively.

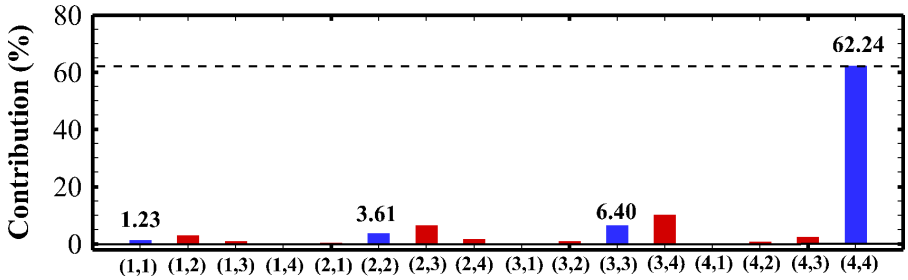

FIG. 27. Decomposition of $C_{h,\mathrm{TH}}$. The diagonal and non-diagonal components are denoted by the blue and red bars, respectively.

the full profile, which peaks at about $y^+ \approx 300$, in good agreement with the outer peak of the complete Reynolds shear stress. This behavior is inconsistent with the findings of Tong *et al.*[11] for the undisturbed turbulent boundary layer. They reported that the full Reynolds shear stress was mainly related to the diagonal component (1, 1) peaking at about $y^+ \approx 20$, which is associated with the small-scale structures of u'' and v'' in the inner region. Combined the vortical structures in Fig. 8 and the spanwise spectra in Fig. 23, we hypothesize that the dominant contribution of the large-scale velocity structures in the outer region to the full Reynolds shear stress is likely linked to the existence of the Görtler-type vortices downstream of the interaction.

In Fig. 25, the decomposition of the wall-normal heat flux is reported, and the sum of the 16 components matches very well with the complete profile. Clearly, a similar trend is also observed, where the predominance of the diagonal component (4, 4) is highlighted in Fig. 25(a), exhibiting close similarities with the original wall-normal heat flux, attaining its peak at $y^+ \approx 438$. Despite such a behavior is consistent with the decomposed results of Tong *et al.*,[11] who also found that the full wall-normal heat flux in the undisturbed boundary layer is dominated by the large-scale outer velocity and temperature structures, we observe that the diagonal component (4, 4) contributes most of the full wall-normal heat flux, whereas the contributions of the other three diagonal components are significantly decreased and can be neglected. This difference will be quantitatively evidenced by the integration in the following analysis. Therefore, it is further confirmed that the wall-normal heat flux in the downstream region strongly depends on the outer large-scale velocity and temperature structures.

Correspondingly, the decompositions of the $C_{h,\mathrm{RS}}$ and $C_{h,\mathrm{TH}}$ contributions are given in Figs. 26 and 27, respectively. Here, all the decomposed components of the Reynolds shear stress and wall-normal heat flux are integrated over the boundary layer to provide more quantitative evidence for the dominance of the large-scale outer turbulent structures. Consistent with the upstream turbulent boundary layer, the four diagonal components contribute most to $C_{f,\mathrm{RS}}$ and $C_{f,\mathrm{TH}}$, reaching about 71.52% and 73.48%, respectively. More specifically, the contribution of the large-scale outer component (4, 4) accounts for

up to about 40% of $C_{f,RS}$ and 62.24% of $C_{f,TH}$. In the previous analysis of Tong *et al.*,[11] corresponding values for component (4, 4) were about 15.40% and 24.97%, respectively. Regarding component (1, 1), the contributions are about 11.03% and 1.23% for $C_{f,RS}$ and $C_{f,TH}$, respectively, compared to 27.52% and 15.86% reported by Tong *et al.*[11] Recalling the significant contributions of $C_{f,RS}$ and $C_{f,TH}$ to the generation of $\bar{C}_h$, the present results quantitatively support the conclusion that the mean WHF generation downstream of the interaction is utterly different from the upstream turbulent boundary layer, where the predominance of the small-scale structures in the near-wall region is overtaken by the large-scale structures in the outer region.

IV. CONCLUSIONS

The wall heat flux signature of supersonic shock wave/turbulent boundary layer interaction has been investigated using data from the DNS of a 33.2° impinging shock wave interacting with a spatially developing boundary layer at $M_\infty = 2.25$ and $Re_\tau = 769$ and a cooled wall condition.

Scaling analysis has shown that the mean WHF scales well with the wall pressure throughout the interaction, except for slight departures. The PDFs normalized by the local RMS value yield a good collapse of the positive tails. The pre-multiplied spectra of the fluctuating WHF evidence that the shock interaction significantly enhances the intermediate frequency dynamics, whereas the low-frequency energy is slightly influenced by the typical low-frequency unsteadiness of the separated shock. The two-point WHF correlations reveal a significant decrease in streamwise coherence in the separation region, followed by a recovery featured by larger streamwise correlation length scales, whereas the spanwise coherence throughout the interaction is relatively unaffected. The convection velocities determined using the space–time correlations of the fluctuating WHF dramatically decrease in the separation region and experience an increase in the downstream region, varying in the range of $0.2–0.5U_\infty$. Decomposition of the mean WHF in the downstream region demonstrates the predominance of the positive $C_{h,RS}$ contribution associated with the Reynolds stress and the negative $C_{h,TH}$ contribution related to turbulent heat transport. The integration of the decomposed Reynolds shear stress and wall-normal heat flux quantitatively reflects the dominant contribution of the large-scale outer velocity and temperature fluctuations, responsible for about 40% of $C_{f,RS}$ and 62.24% of $C_{f,TH}$.

ACKNOWLEDGMENTS

This study was supported by the National Natural Science Foundation of China (Nos. 11972356 and 91852203) and the National Key R&D Program of China (No. 2019YFA0405300).

AUTHOR DECLARATIONS

Conflict of Interest

The authors have no conflicts to disclose.

DATA AVAILABILITY

Some or all data, models, and code generated or used during the study are available from the corresponding author upon reasonable request (siwei.dong@cardc.cn).

REFERENCES

[1]D. S. Dolling, "Fifty years of shockwave/boundary layer interaction research: What next?," AIAA J. **39**(8), 1517–1531 (2001).
[2]D. V. Gaitonde, "Progress in shock wave/boundary layer interactions," Prog. Aerosp. Sci. **72**, 80–99 (2015).
[3]D. M. Bushnell and L. M. Weinstein, "Correlation of peak heating for reattachment of separated flows," AIAA J. **5**(9), 1111–1112 (1968).
[4]L. H. Back and R. F. Cuffel, "Changes in heat transfer from turbulent boundary layers interacting with shock waves and expansion waves," AIAA J. **8**(10), 1871–1873 (1970).
[5]N. Murray, R. Hillier, and S. Williams, "Experimental investigation of axisymmetric hypersonic shock wave/turbulent boundary layer interactions," J. Fluid Mech. **714**, 152–189 (2013).
[6]E. Schülein, "Skin-friction and heat flux measurements in shock/boundary-layer interaction flows," AIAA J. **44**(8), 1732–1741 (2006).
[7]Y. Lee, G. S. Settles, and C. C. Horstman, "Heat transfer measurements and computations of swept shock wave/boundary layer interactions," AIAA J. **32**(4), 726–734 (1994).
[8]A. A. Pasha and K. A. Juhany, "Numerical simulation of compression corner flows at Mach number 9," Chin. J. Aeronaut. **33**(6), 1611–1624 (2020).
[9]Z. F. Li, Z. Y. Zhang, J. Wang, and J. M. Yang, "Pressure-heat flux correlations for shock interactions on V-shaped blunt leading edges," AIAA J. **57**(10), 4588–4592 (2019).
[10]D. Sun, Q. L. Guo, X. X. Yuan, H. Y. Zhang, and C. Li, "A decomposition formula for the wall heat flux of a compressible boundary layer," Adv. Aerodyn. **3**, 33 (2021).
[11]F. L. Tong, S. W. Dong, J. Lai, X. X. Yuan, and X. L. Li, "Wall shear stress and wall heat flux in a supersonic turbulent boundary layer," Phys. Fluids **34**, 015127 (2022).
[12]M. Bernardini, I. Asproulias, J. Larsson, S. Pirozzoli, and F. Grasso, "Heat transfer and wall temperature effects in shock wave turbulent boundary layer interactions," Phys. Rev. Fluids **1**, 084403 (2016).
[13]S. Priebe, J. H. Tu, C. W. Rowley, and M. P. Marin, "Low-frequency dynamics in a shock-induced separated flow," J. Fluid Mech. **807**, 441–477 (2016).
[14]P. Dupont, C. Haddad, and J. F. Debieve, "Space and time organization in a shock-induced separated boundary layer," J. Fluid Mech. **559**, 255–277 (2006).
[15]S. Priebe and M. P. Martin, "Low-frequency unsteadiness in shock wave-turbulent boundary layer interaction," J. Fluid Mech. **699**, 1–49 (2012).
[16]P. S. Volpiani, M. Bernardini, and J. Larsson, "Effects of a nonadiabatic wall on supersonic shock/boundary layer interactions," Phys. Rev. Fluids **3**, 083401 (2018).
[17]S. Pirozzoli, F. Grasso, and T. B. Gatski, "Direct numerical simulation and analysis of a spatially evolving supersonic turbulent boundary layer at M = 2.25," Phys. Fluids **16**, 530 (2004).
[18]J. Fang, A. A. Zheltovodov, Y. F. Yao, C. Moulinec, and D. R. Emerson, "On the turbulence amplification in shock-wave/turbulent boundary layer interaction," J. Fluid Mech. **897**, A32 (2020).
[19]V. Pasquariello, S. Hickel, and N. A. Adams, "Unsteady effects of strong shock-wave/boundary-layer interaction at high Reynolds number," J. Fluid Mech. **823**, 617–657 (2017).
[20]F. L. Tong, X. L. Li, Y. H. Duan, and C. P. Yu, "Direct numerical simulation of supersonic turbulent boundary layer subjected to a curved compression ramp," Phys. Fluids **29**, 125101 (2017).
[21]F. L. Tong, X. L. Li, X. X. Yuan, and C. P. Yu, "Incident shock wave and supersonic turbulent boundary layer interactions near an expansion corner," Comput. Fluids **198**, 104385 (2020).
[22]F. L. Tong, J. Y. Duan, and X. L. Li, "Direct numerical simulation of impinging shock wave and turbulent boundary layer interaction over a wavy-wall," Chin. J. Aeronaut. **34**(5), 350–363 (2021).
[23]M. P. Martin, E. M. Taylor, M. Wu, and V. G. Weirs, "A bandwidth-optimized WENO scheme for the effective direction numerical simulation of compressible turbulence," J. Comput. Phys. **220**, 270–289 (2006).
[24]M. Wu and M. P. Martin, "Direct numerical simulation of supersonic turbulent boundary layer over a compression ramp," AIAA J. **45**(4), 879–889 (2007).
[25]S. Gottieb and C. W. Shu, "Total variation diminishing Runge–Kutta schemes," Math. Comput. **67**, 73–85 (1998).

[26]T. J. Poinsot and S. K. Lele, "Boundary conditions for direct simulations of compressible viscous reacting flows," J. Comput. Phys. **101**, 104–129 (1992).
[27]F. L. Tong, J. Y. Duan, and X. L. Li, "Characteristics of wall-shear stress fluctuations in shock wave and turbulent boundary layer interaction," J. Turbul. **22**, 761–783 (2021).
[28]M. Elena and J. P. Lacharme, "Experimental study of a supersonic turbulent boundary layer using a laser Doppler anemometer," J. Mech. Theor. Appl. **7**, 175–190 (1988).
[29]S. Pirozzoli, M. Bernardini, and F. Grasso, "Characterization of coherent vertical structures in a supersonic turbulent boundary layer," J. Fluid Mech. **613**, 205–231 (2008).
[30]M. B. Sun, N. D. Sandham, and Z. W. Hu, "Turbulence structures and statistics of a supersonic turbulent boundary layer subjected to concave surface curvature," J. Fluid Mech. **865**, 60–99 (2019).
[31]P. Schlatter and R. Örlü, "Assessment of direct numerical simulation data of turbulent boundary layers," J. Fluid Mech. **659**, 116–126 (2010).
[32]J. Jeong and F. Hussain, "On the identification of a vortex," J. Fluid Mech. **285**, 69–94 (1995).
[33]S. Pirozzoli and F. Grasso, "Direct numerical simulation of impinging shock wave/turbulent boundary layer interaction at M = 2.25," Phys. Fluids **18**, 065113 (2006).
[34]S. Priebe and M. P. Martin, "Turbulence in a hypersonic compression ramp flow," Phys. Rev. Fluids **6**, 034601 (2021).
[35]S. Grosse and W. Schroder, "Wall-shear stress patterns of coherent structures in turbulent duct flow," J. Fluid Mech. **633**, 147–158 (2009).
[36]B. Nottebrock, K. J. Geurts, and W. Schroder, "Wall-shear stress measurements in an adverse pressure gradient turbulent boundary layer," AIAA Paper No. 2014-2098, 2014.
[37]K. R. Sreenivasan and R. A. Antonia, "Properties of wall shear stress fluctuations in a turbulent duct flow," J. Appl. Mech. **44**, 389–395 (1977).
[38]M. Bernardini, S. Pirozzoli, and F. Grasso, "The wall pressure signature of transonic shock/boundary layer interaction," J. Fluid Mech. **671**, 288–312 (2011).
[39]L. Duan, M. M. Choudhari, and C. Zhang, "Pressure fluctuations induced by a hypersonic turbulent boundary layer," J. Fluid Mech. **804**, 578–607 (2016).
[40]C. Cheng, W. P. Li, A. L. Duran, and H. Liu, "Identity of attached eddies in turbulent channel flows with bidimensional empirical mode decomposition," J. Fluid Mech. **870**, 1037–1071 (2019).
[41]Y. Zhuang, H. J. Tan, X. Li, F. J. Sheng, and Y. C. Zhang, "Görtler-like vortices in an impinging shock wave/turbulent boundary layer interaction flow," Phys. Fluids **30**, 061702 (2018).